Available online at www.sciencedirect.com
ScienceDirect
Ceramics International 35 (2009) 2047–2051
CERAMICS INTERNATIONAL
www.elsevier.com/locate/ceramint

Impedance spectroscopic behaviour of spark plasma sintered nanocrystalline scandia stabilized zirconia (SSZ)

Koushik Biswas

Department of Metallurgical and Materials Engineering, Indian Institute of Technology, Kharagpur 721302, India

Received 28 August 2008; received in revised form 23 September 2008; accepted 10 November 2008
Available online 3 December 2008

Abstract

Nanocrystalline scandia (Sc_2O_3) doped zirconia was prepared by dissolution and co-precipitation method. The formation of the nanostructured nearly cubic phase has been observed from transmission electron microscope and X-ray diffraction studies. Spark plasma sintering retains the nano/submicrograin structure. The frequency dependent conductivities were measured in the frequency range from 100 Hz to 1 MHz and at temperatures 300–800 K. The impedance diagram shows the grain interior and grain boundary resistance contributions. The frequency dependent conductance spectra show the DC plateau (at low frequency region) and dispersive region suggesting the correlated hopping motion of ions. The dielectric-loss spectra suggest the presence dielectric relaxation, which is related to enthalpy of ion hopping. Characteristic hopping frequencies were calculated and appear to be related to the thermally activated ion hoping process.

Keywords: C. Impedance; Spark plasma sintering; Nano-zirconia; Dielectric behaviour; Hopping frequencies

1. Introduction

ZrO_2-based solid electrolytes, which are good oxygen-ion conductors are of particular interest for application in high-temperature solid oxide fuel cells, oxygen separation membranes and sensors [1–6]. At high temperatures, pure ZrO_2 reveals the cubic fluorite structure and provides high oxide ion conductivity leading to development of solid oxide fuel cell (SOFC) electrolyte materials. At present, the most advanced SOFCs are based on yttria stabilized zirconia (YSZ) electrolytes, Ni–YSZ cermets as anode and LSM (strontium doped lanthanum manganate) as cathode material [5]. Several studies have been carried out to improve the performance of the electrolyte by using ceria doped with rare earth oxides as an electrolyte, or replacing yttria with scandia (Sc_2O_3) or alkali rare earth oxides for stabilizing zirconia electrolyte. Apart from materials aspect, process parameters and routes were also major concern for the researchers to improve the overall performance of the fuel cells. Torrens et al. [7] explored the effects of synthesis routes including solid-state reaction and co-precipitation on sinterability and electrical properties of polycrystalline CGO (gadolinium oxide doped ceria) and reported a remarkable improvement in performance of the electrolyte produced through the wet chemical method. However, only limited amount of activities concerning the influence of various synthesis processes on sintering and electrical behaviour of the ceramic electrolytes have been done so far. In fact, the studies to-date, have mostly confined in SOFCs based on YSZ as the electrolyte. Recently, it is suggested that the efficiency of ionic conduction and chemical/thermal stability of the electrolyte could be significantly enhanced if scandia stabilized zirconia in the nanocrystalline state is used instead of conventional YSZ. The conductivity enhancement in the scandia stabilized zirconia (SSZ) material is attributed to the minimal difference in ionic radii of the host Zr and dopant Sc [8]. The activation energy for the transport of oxygen ions in the SSZ materials is also reduced as compared to the YSZ material [8]. There is a strong interest in the SSZ materials, primarily motivated by improved conductivity, and a number of groups, specifically in Japan, are pursuing active research efforts [1,9,10]. A number of different approaches can be employed to enhance conductivity of the bulk electrolyte [11]. The aforementioned SSZ materials were developed by the technique of homogeneous doping in which the host zirconium sites are replaced by scandium sites. Thus, the present investigation will aim on

---

E-mail address: k4biswas@yahoo.com.

0272-8842/$34.00 © 2008 Elsevier Ltd and Techna Group S.r.l. All rights reserved.
doi:10.1016/j.ceramint.2008.11.009

Table 1
Characteristics of the starting powder.

Powder	Manufacturer	Chemical analysis (wt%)
$ZrOCl_2 \cdot 8H_2O$	LOBA Chemicals, India	Purity, 99.95%; Ti–0.01%
Sc_2O_3	STERM Chemicals, USA	Purity, 99.9% (Sc)

synthesis of nanocrystalline scandia stabilized zirconia electrolyte by a novel wet chemical route, consolidating by spark plasma sintering process and study the ion dynamics on this system. The AC impedance spectroscopy technique is an excellent tool to analyze the ionic conduction, since it gives the microscopic view of ion transport mechanisms.

2. Experimental procedure

The starting materials used to fabricate green pellets of 8 mol% Sc_2O_3 stabilized zirconia (8-SSZ) are commercially available $ZrOCl_2 \cdot 8H_2O$ and Sc_2O_3 powders. The characteristics of these powders and their specifications are tabulated in Table 1.

In order to prepare the powder premixes, $ZrOCl_2 \cdot 8H_2O$ was dissolved in distilled water at room temperature. Sc_2O_3 was dissolved in hot concentrated HCl. The formula mass ratios will be determined by weighing the resulting oxides mass obtained after calcinations of a known amount of precursor. Precipitation of the powder was done using aqueous 5% NH_4OH solution (maintaining pH value within 9–10) as the hydrolyzing agent. This wet chemical method was adopted to achieve atomistic mixing of ZrO_2 and Sc_2O_3 powders. The precipitate was rinsed thoroughly with distilled water and dried overnight in an oven at 110 °C. The resultant agglomerates were ground into powder using the mortar and pestle. The powders were then calcined at 900 °C for 2 h in air. After calcinations, the powders were ground. Sintering was done in a spark plasma sintering furnace at 1350 °C for 5 min under vacuum at a pressure of 60 MPa keeping heating rate at 500 °C/min. In order to estimate the exact temperature profile inside the graphite die and specimen, some small numerical calculations was done using ABAQUS and MATLAB software based on linear steady state thermo-electrical couple approach.

Microstructures of the calcined powder and sintered specimens were examined with scanning electron microscope (ZEOL, Japan) and transmission electron microscope (CM-12, Phillips, Holland). The qualitative phase analysis was done by X-ray diffraction (PW 1840 diffractometer control, Phillips, Holland) using filtered Cu Kα radiation with a wavelength of $\lambda = 1.54$ Å and then by comparing the X-ray diffraction patterns with the JCPDS standards. The calcined and sintered specimens are ground to fine powders in order to avoid any texturing effects. The particle size (D) was also estimated from XRD plots using the Debye Scherrer's formula:

$$D = \frac{0.94\lambda}{\cos\theta_B (B^2 - b^2)^{1/2}} \qquad (1)$$

where λ is the wavelength of the characteristic X-ray, B and b are the full-width at half-maximum of the corresponding XRD peak of strain free and sintered/calcined sample, respectively.

For electrical characterization, sample pellet was contacted by first sputtering of ~50 nm Pt layer followed by coating with platinum paste and heat-treated at 1100 °C for 1 h to burn out the binder of the platinum paste. AC impedance measurement was performed using HIOKI 3532 LCR, HiTester, Japan in the temperature range of 50–500 °C at various frequency level (from 100 Hz to 1 MHz).

3. Results and discussion

3.1. Microstructure and phase analysis

Transmission electron microscopic (TEM) image of the 8-SSZ nano-particles, as shown in Fig. 1, shows that the particles are highly crystalline and have a uniform size distribution with a mean particle size of ~17 nm. The selected area diffraction patterns (inset) also corroborate the existence of nanocrystalline powder. Fig. 2 shows the XRD patterns obtained from the calcined and sintered specimen. It is noted that in the 8-SSZ specimen, all peaks can be assigned on the basis of a cubic structure. As the tetragonal ($P4_2/nmc$) phase is slightly distorted from the cubic phase ($Fm\bar{3}m$) and peaks are broadened from the nano-particle size, it is very difficult to differentiate between

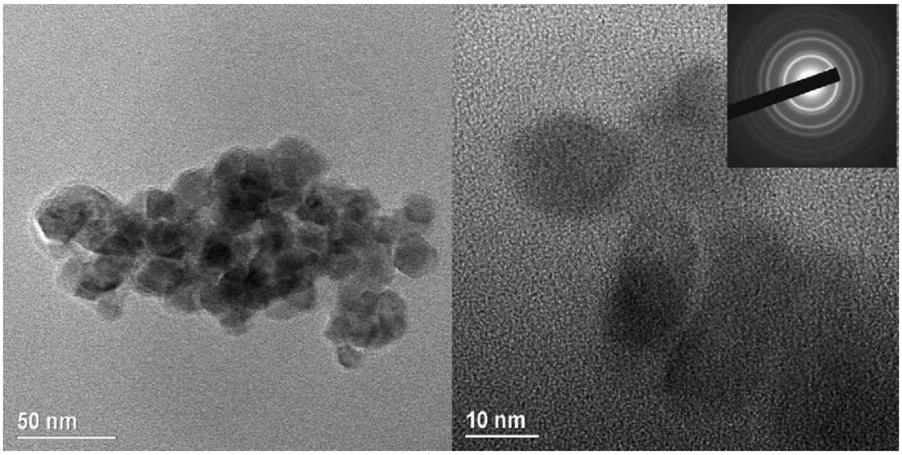

Fig. 1. Transmission electron micrographs of 8-SSZ nanocrystals showing the selected area diffraction pattern (inset).

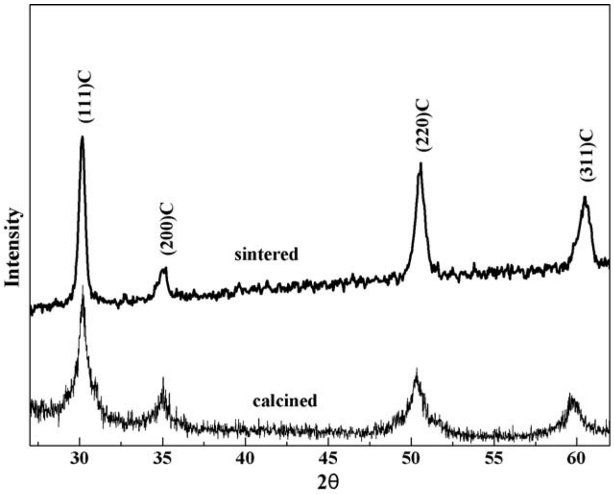

Fig. 2. X-ray diffraction pattern of 8-SSZ powders after calcinations and sintering.

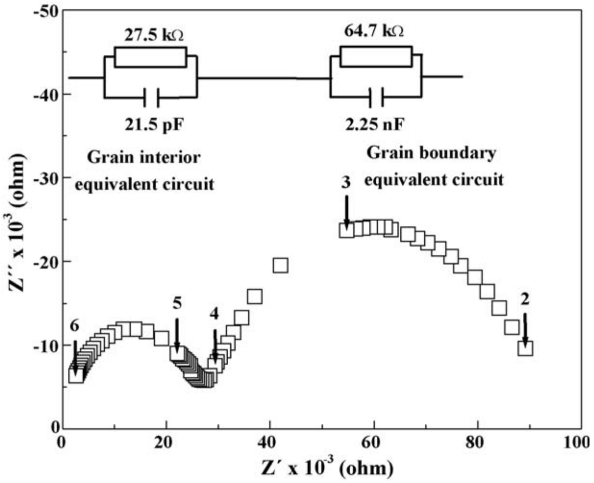

Fig. 4. Complex impedance spectrum and equivalent circuit of nanocrystalline sintered 8-SSZ at 350 °C. The numbers indicate the logarithm of measuring frequencies.

these two crystal phases using the X-ray diffraction pattern. However several authors have reported the presence of both tetragonal and cubic phases [8,10]. The phase diagram in the ZrO_2–Sc_2O_3 system [12] predicts the existence of a monoclinic phase if the specimen is cooled under equilibrium conditions. However, the 8-SSZ specimen processed under similar conditions does not show the presence of the monoclinic phase. The average crystallite and the grain sizes for calcined and sintered samples were also determined using Scherrer's formula (Eq. (1)) and they are found to be 38.5 ± 4.3 nm and 83.6 ± 9.2 nm, respectively. The SEM image of sintered 8-SSZ (Fig. 3) shows the presence homogeneously distributed faceted grains with an average grain size $<\sim$100 nm.

3.2. *Electrical characterizations*

3.2.1. *Impedance analysis*

Fig. 4 shows the impedance plot of 8-SSZ sample measured at 350 °C. The equivalent electric circuit (shown in Fig. 4) for a complex impedance plot is a parallel resistor and a constant phase element (CPE) circuit [13]. The impedance Z (or admittance $Y = 1/Z$) of such an equivalent circuit is given by

$$Z = R_0\left[1 + (\omega\tau_R)^n \cos\left(\frac{n\pi}{2}\right) + j(\omega\tau_R)^n \sin\left(\frac{n\pi}{2}\right)\right] \quad (2)$$

where τ_R (=1/f_R (*relaxation frequency*)) is the time constant and R_0 is the resistance of the circuit. The parameter n is related to the depression angle θ of the impedance semicircle and can be estimated by $1 - 2\theta/\pi$. The circular fitting of the complex impedance plot by using the program EQ developed by Boukamp [14,15] yields the grain interior resistance (R_{gi}) and grain boundary resistance (R_{gb})(blocking effect) due to internal interfaces (grain boundaries and porosity). The high-frequency semicircle has been attributed to the grain interior resistance and the low-frequency semicircle is due to grain boundary resistance. The large difference in time constants allows the grain interior resistance semicircle to be clearly separated from that of the grain boundary curve. The associated capacitance values are calculated using the relation $2\pi f_R$ RC = 1 and they are found to be in the order of pF and nF, which indicates the nature of the semicircles as grain interior and grain boundary [16]. The depression angle for the bulk semicircle was always lower than 5° indicating a good homogeneity of the electrical properties of the grains and therefore of their composition. The blocking process depressions were found to vary between 10° and 12°, which were at the lower side, demonstrating a small broadening of the blocking characteristics [16]. The value of n calculated for the 8-SSZ specimen within the temperature range of 300–400 °C is about 0.88 ± 0.04. For different temperatures, the bulk, DC and the blocking conductivities were estimated using admittance plane (Fig. 5). The temperature dependence of the conductivity follows an Arrhenius type of behaviour and the activation enthalpy for conduction was found to be 128.5 ± 2 kJ/mol. Activation energies corresponding to blocking effect and DC conduction were also obtained and highlighted in Fig. 6. The observed activation energies are almost similar found by other researchers [9,17–19].

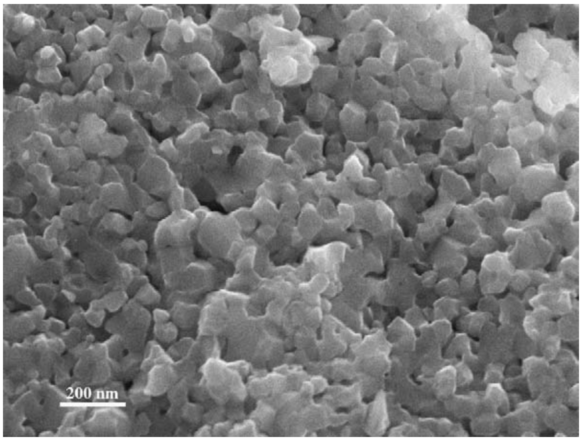

Fig. 3. Scanning electron micrographs of 8-SSZ sintered at 1200 °C for 1 h.

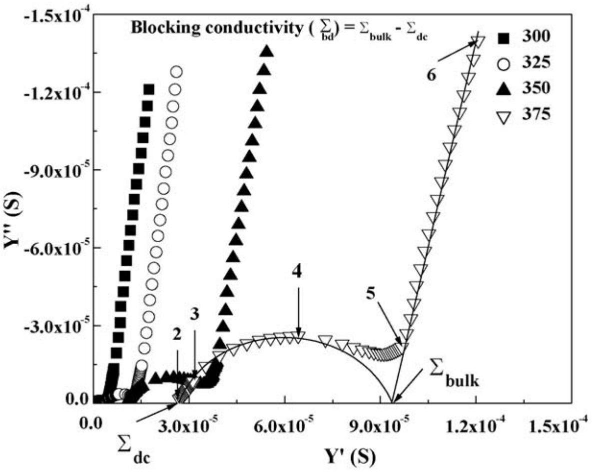

Fig. 5. Admittance diagram of sintered 8-SSZ showing the bulk, dc and the blocking conductance at different temperatures. The numbers indicate the logarithm of measuring frequencies.

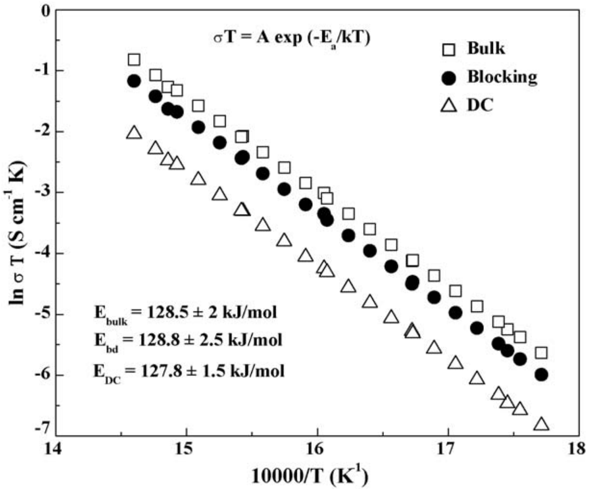

Fig. 6. Arrhenius plot of bulk, block and dc conductance of 8-SSZ showing the different activation energies.

3.2.2. Characteristic hopping frequencies

Almond, West and co-workers derived an expression for the AC conductivity (frequency dependent conductivity) of an ionic conductor, $\sigma(\omega)$ [20–23], using Jonscher's universal expression [24]:

$$\sigma(\omega) = K f_{\mathrm{P}}\left[1 + \left(\frac{\omega}{f_{\mathrm{P}}}\right)^{n}\right] \tag{3}$$

and noted that

$$\text{DC conductivity} = \sigma_{\mathrm{DC}} = K f_{\mathrm{P}} \tag{4}$$

where f_{P} is the hopping rate, referred as the 'Almond–West hopping frequency'. Barton–Nakjima–Namikawa (BNN) relation [25] shows that DC conductivity in ionic conductors is proportional to the hopping rate of the charge carriers. The hopping of the charge carriers can result in a dielectric loss peak and the DC conductivity is also proportional to the loss peak frequency (f_{d}). Therefore, one can write:

$$\sigma_{\mathrm{DC}} = p\varepsilon_0 \Delta\varepsilon f_{\mathrm{d}} = A f_{\mathrm{d}} = K f_{\mathrm{P}} \tag{5}$$

where p is a factor ~1, ε_0 is the dielectric constant for vacuum and $\Delta\varepsilon$ is the magnitude of the dielectric loss associated with ion hopping. It is also noted that, the relaxation frequency (f_{R}) frequency has the following relationship with the Almond–West hopping frequency f_{P}:

$$\left(\frac{f_{\mathrm{P}}}{f_{\mathrm{R}}}\right)^{n} \cos\left(\frac{n\pi}{2}\right) = 1 \tag{6}$$

So, the three characteristics frequencies (f_{R}, f_{P} and f_{d}) for thermally activated ion hopping process are someway related to each other.

The frequency dependence of the conductivity at different temperatures was plotted in Fig. 7. According to Eq. (3), the DC conductivity (σ_{DC}), Almond–West hopping frequency (f_{P}), and the exponential constant n, can be obtained by universal conductivity law means of curve fitting. But the frequency range of applicability of this expression is rather small due to the influence of the grain boundary relaxation and does not allow a reliable determination of parameters. However, excluding the frequency dependent part of the grain boundary or other extrinsic relaxation effects will lead to somewhat better accuracy. In Fig. 7, each curve displays a low-frequency plateau, which corresponds to the DC conductivity of the bulk material, and a dispersive region at high frequency, which corresponds to the AC conductivity. The existence of such a dispersive regime in the conductivity rules out the possibility that mobile ions perform a random hopping and reveals that the ionic motion is somehow correlated [26]. The value of n determined by curve fitting is 0.8 ± 0.15, which is fairly close to the value obtained by semicircular fitting of the impedance spectra.

The dielectric relaxation frequencies (f_{d}) were determined from the dielectric-loss behaviour (Fig. 8). This will be

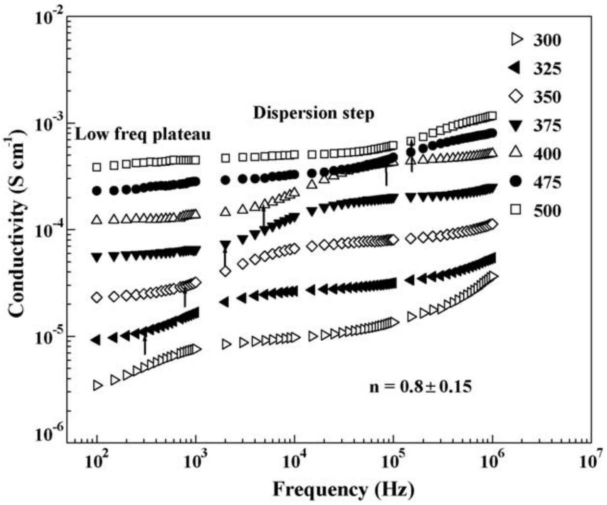

Fig. 7. Frequency dependent conductivity spectra at various temperatures for 8-SSZ. Arrows indicate the grain boundary relaxation frequencies.

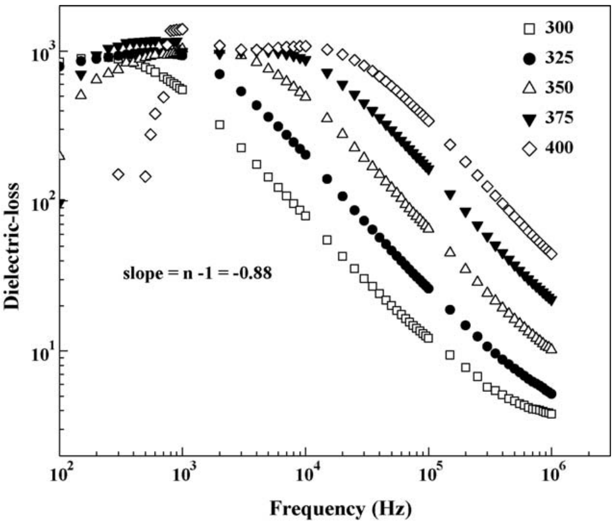

Fig. 8. Dielectric-loss behaviour of 8-SSZ showing a constant peak height at $\chi'' = 10^3$.

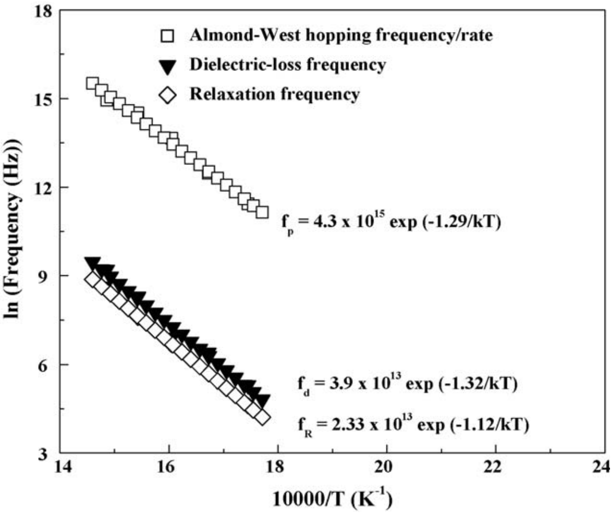

Fig. 9. Arrhenius plot of the characteristic frequencies: peak (relaxation) frequency for Z'', Almond–West's hopping frequency and dielectric loss peak frequency.

obtained from the relationship:

$$\text{Dielectric loss} = \chi'' = \frac{\sigma_{AC} - \sigma_{DC}}{\omega\varepsilon_0} \tag{7}$$

Eq. (7) is expected to be proportional to ω^{n-1} above the dielectric relaxation frequency (f_d). The peak heights determined for all temperatures are quite similar, at $\sim 10^3$. The value of n found was quite lower ($\sim$0.12) than the value obtained by earlier two methods. The discrepancy suggests that the curve fitting carried out earlier was done over the complete frequency range unlike the dielectric loss graph, where the linear relationship was satisfied only over a limited frequency range. On the other hand, this kind of anomaly suggests that the complex impedance plot is not exactly semicircular (following brick-layer model), and the universal expression is only approximately satisfied in the present system.

The three characteristic frequencies (f_R, f_P and f_d) were plotted in Fig. 9. The activation energy for hopping is found to be 1.29 eV. The pre-exponential terms for f_R and f_d are comparable and these frequencies are attributed to vibration frequencies in crystals [27]. However, Namikawa [25] assigned f_d to a hopping relaxation mechanism. Several authors [24,25,27] reported that the relaxation process is closely related to the hopping behaviour of ionic conductors. As a consequence, the activation energy for corresponding to the three frequencies can be attributed to the migration enthalpy of the charge carriers.

4. Conclusions

Nanometric scandia stabilized zirconia-based electrolyte materials can be synthesized and sintered up to full densification without much grain coarsening. Frequency dependent conductivity can be well described using universal dielectric response, however anomaly in dielectric behaviour and discrepancy in exponential factor suggest the limitation of brick-layer model. The three characteristic frequencies appear to be related to the thermally activated ion hoping process.

References

[1] Y. Mizutani, M. Tamura, M. Kawai, O. Yamamoto, Solid State Ionics 72 (1994) 271.
[2] I. Tatsumi, M. Hideaki, T. Yusaku, Solid State Ionics 79 (1995) 147.
[3] S. Wang, H. Inada, H. Tagawa, M. Dokiya, T. Hashimoto, Solid State Ionics 107 (1997) 73.
[4] A. Tsoga, A. Gupta, A. Naoumidis, P. Nikolopoulos, Acta Mater. 18–19 (2000) 4709.
[5] J.-H. Kim, H.-I. Yoo, Solid State Ionics 140 (2001) 105.
[6] Z. Cai, T.N. Lan, S. Wang, M. Dokiya, Solid State Ionics 152–153 (2002) 583.
[7] R.S. Torrens, N.M. Sammes, G.A. Tompsett, Solid State Ionics 111 (1998) 9.
[8] O. Yamamoto, Y. Arati, Y. Takeda, N. Imanishi, Y. Mizutani, M. Kawai, Y. Nakamura, Solid State Ionics 79 (1995) 137.
[9] Y. Arachi, H. Sakai, O. Yamamoto, Y. Takeda, N. Imanishai, Solid State Ionics 121 (1999) 133.
[10] M. Hirano, S. Watanabe, E. Kato, Y. Mizutani, M. Kawai, Y. Nakamura, Solid State Ionics 111 (1998) 161.
[11] C. Varanasi, C. Juneja, C. Chen, B. Kumar, J. Power Sources 147 (2005) 128.
[12] F.M. Spiridonov, L.N. Popova, R.Ya. Popilskii, J. Solid State Chem. 2 (1970) 430.
[13] J.R. Macdonald, Impedance Spectroscopy: Emphasizing Solid Materials and Systems, John Wiley, New York, 1987.
[14] B.A. Boukamp, Solid State Ionics 20 (1986) 301.
[15] B.A. Boukamp, Solid State Ionics 18–19 (1986) 136.
[16] J.T.C. Irvine, D.C. Sinclair, A.R. West, Adv. Mater. 2 (1990) 138.
[17] S.P.S. Badwal, F.T. Ciacchi, D. Milosevic, Solid State Ionics 136–137 (2000) 91.
[18] R.J. Stafford, S.J. Rothman, J.L. Routbort, Solid State Ionics 37 (1990) 67.
[19] M.V. Inozemtser, M.V. Perfil'ev, V.P. Gorelov, Elecktrokhimiya 12 (1976) 1231.
[20] D.P. Almond, O.K. Duncan, A.R. West, Solid State Ionics 8 (1983) 159.
[21] D.P. Almond, A.R. West, Solid State Ionics 9–10 (1983) 277.
[22] D.P. Almond, A.R. West, R.J. Grant, Solid State Commun. 44 (1982) 1277.
[23] D.P. Almond, C.C. Hunter, A.R. West, J. Mater. Sci. 19 (1984) 3236.
[24] A.K. Jonscher, Nature 267 (1977) 673.
[25] H. Namikawa, J. Non-Crsyt. Solids 18 (1975) 173.
[26] K. Funke, Prog. Solid State Chem. 22 (1993) 111.
[27] J. Luo, E.F. Hairetdinov, D.P. Almond, R. Stevens, Solid State Ionics 122 (1999) 205.